Please verify that (1) all pages are present, (2) all figures are acceptable, (3) all fonts and special characters are correct, and (4) all text and figures fit within the margin lines shown on this review document. Return to your MySPIE ToDo list and approve or disapprove this submission.

Tomographic reconstruction of the pulse-echo spatiotemporal impulse response

Nghia Q. Nguyen,[a] Craig K. Abbey,[d] Rebecca D. Yapp,[b] and Michael F. Insana[a,b,c]

[a]Department of Electrical and Computer Engineering, [b]Department of Bioengineering
[c]Beckman Institute for Advanced Science and Technology,
University of Illinois at Urbana-Champaign, USA
[d]Department of Psychology, University of California at Santa-Barbara, USA

ABSTRACT

Virtually every area of ultrasonic imaging research requires accurate estimation of the spatiotemporal impulse response of the instrument, and yet accurate measurements are difficult to achieve. The impulse response can also be difficult to predict numerically for a specific device because small unknown perturbations in array properties can generate significant changes in predicted pulse-echo field patterns. A typical measurement for a 1-D array transducer employs a line scatterer oriented perpendicular to the scan plane. Echoes from line scatterers located throughout the field of view constitute estimates of shift-varying line response functions. We propose an inverse-problem approach to the reconstruction of point-spread functions from line-spread functions. A collection of echoes recorded for a range of line-scatterer rotation angles are treated as projections of sound pressure onto the transducer array surface. Although the reconstruction is mathematically equivalent to filtered backprojection, it provides significant advantages with respect to interpolation that confound straightforward implementations. Field II predictions used to model measurements made on commercial systems suggest the reconstruction accuracy is with 0.32% for noiseless echo data. Application of the method to data acquired from a commercial system are evaluated from the perspective of deconvolution.

Keywords: ultrasonic imaging, computerized tomography, inverse problems, impulse response reconstruction

1. INTRODUCTION

The performance of an ultrasonic imaging system for any application is fundamentally limited by its ability to successfully concentrate sound energy at all points in the field of view and at each instant of time. The temporal bandwidth of the electronics–transducer assembly, the active apertures applied during transmission and reception, and element delays and weights are *beamforming* properties that contribute to essential performance metrics — the spatial and contrast resolutions of the system.[1] System designers striving to assess and improve performance[2–4] need to accurately measure the impulse response throughout the field.

The simplest measurements are obtained in the scan plane from local autocovariance estimates applied to fully-developed image speckle.[5] Coherent summation of reflected pressure waves measured at the transducer surface from randomly distributed scattering media results in B-mode speckle whose dimensions indicate in-plane spatial resolution, but only under the limiting conditions where maximum coherence is achieved. It is well known that speckle correlation lengths for off-focus field locations and conditions that distort pulse phases, e.g., aberrating media, underestimate the spatial extent of the impulse response and provide no direct phase information.

Better IR estimates for 1-D arrays are obtained from radio-frequency (RF) signals of a line-scatterer reflection, provided the scattering material does not acoustically resonate near the carrier frequency. Beam profile phantoms with line scatterers are commercially available, e.g., ATS #539 (ATS Industries, Bridgeport CT). The echo pattern appears as a point response in the scan plane, but is actually a line-spread function

For further information, send correspondence to {nnguyen6,mfi}@illinois.edu

SPIE USE: ____ DB Check, ____ Prod Check, Notes:

Please verify that (1) all pages are present, (2) all figures are acceptable, (3) all fonts and special characters are correct, and (4) all text and figures fit within the margin lines shown on this review document. Return to your MySPIE ToDo list and approve or disapprove this submission.

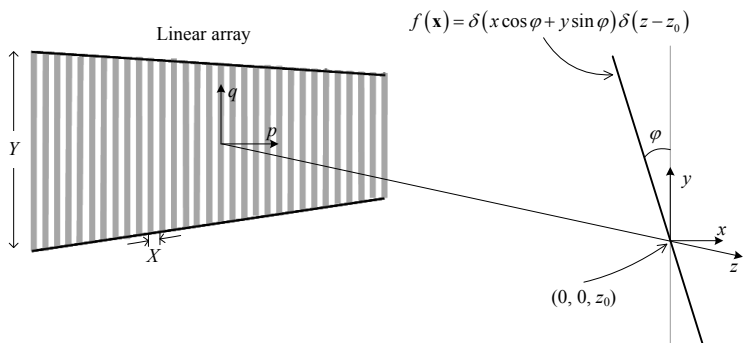

Figure 1. Geometry of the linear array and line scatterer (represented as Dirac deltas) are illustrated. The array coordinates p, q are sampled on the spatial intervals X, Y respectively. The line scatterer, with coordinates x, y, z, is rotated in the x, y plane about the z axis with angle φ.

(lsf), which is the impulse response integrated over the elevational dimension of the transducer aperture. Depending on the elevational beamwidth, the lsf may or may not be a good approximation of the point-spread function (psf).

In this paper, we proposed a method for estimating pulse-echo impulse responses by processing echoes obtained from a line scatterer rotated in a plane normal to the beam axis, Fig 1. Applying a linear pulse-echo model of echo formation, lsf echoes are shown to yield projections of the sound beam that may be reconstructed to estimate the impulse response. Projections are linear transformations of the impulse response along lines in space. Reconstruction from projections is an inverse problem that can be solved through application of *singular value decomposition* (SVD) as described by Barrett and Myers.[6] Our approach has similarities to standard filtered backprojection used in photon transmission or emission tomography,[7] but a major geometric difference is that the detector (1-D array) does not rotate with the projection source (line scatterer). Pulse-echo projections from 1-D arrays contain a large null space that limits reconstruction accuracy.

The paper is organized as follows. Section 2 describes the forward problem whereby pulse-echo signals are formed from the line-scatterer geometry of Fig 1. Section 3 describes an inverse-problem approach to reconstructing the transducer impulse response from the projections illustrated in Fig 2. Section 4 applies the method to simulated and experimental data. Success of the reconstructions for echo simulations is determined through comparisons with the underlying model, whereas experimental validation is made through echo deconvolution. Section 5 summarizes and concludes findings of the study.

2. BACKGROUND

Zemp et al.[8] modeled the formation of RF echo signals g as a linear system given by

$$g(\mathbf{t}) = \int d\mathbf{x}\; h(\mathbf{x}, \mathbf{t}) f(\mathbf{x}) + n(\mathbf{t}) \; . \tag{1}$$

Scattering function f is represented in object space at vector position $\mathbf{x} = (x, y, z)$. Object functions are linearly mapped into data g recorded at acquisition-time-dependent vector $\mathbf{t} = (t_1, t_2, t_3)$ through the pulse-echo spatiotemporal impulse response h. Function n is signal-independent, white Gaussian noise originating from the measurement process. Echo acquisition is a mapping of spatial objects into temporal data, while B-mode image formation restores the spatial context for human interpretation. To reconstruct h from g projections we must first describe essential space-time relationships among objects, RF data, and images.

Echo data are acquired as a sequential linear array, first along range time t_1 to yield an A-line, then along cross-range time t_2 to yield a frame, but the acquisition may be extended to "elevational time" t_3 for dynamic imaging or volumetric acquisitions. The total acquisition time is $t = t_1 + t_2 + t_3$. Echoes are sampled in range

SPIE USE: ____ DB Check, ____ Prod Check, Notes:

Please verify that (1) all pages are present, (2) all figures are acceptable, (3) all fonts and special characters are correct, and (4) all text and figures fit within the margin lines shown on this review document. Return to your MySPIE ToDo list and approve or disapprove this submission.

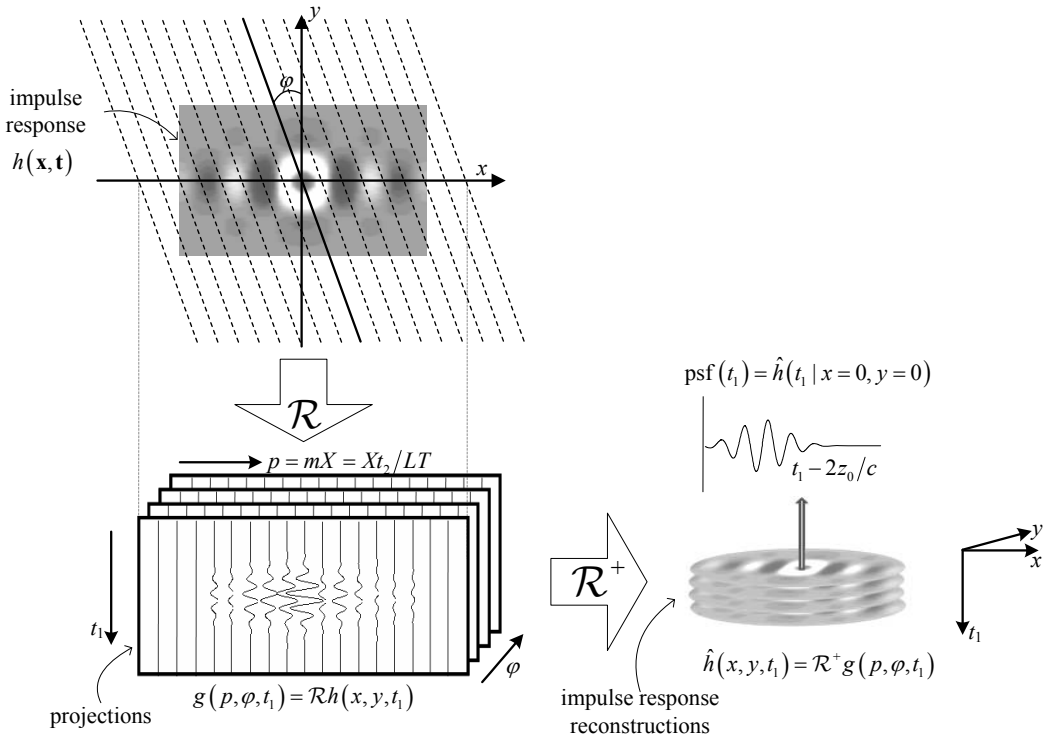

Figure 2. Geometry used to acquire echo projections and reconstruct the impulse response. Positioning a line scatterer in the x, y plane at depth $z = z_0$, we explore $h(x, y, t_1|z_0, t_2, t_3)$ abbreviated as $h(x, y, t_1)$. Rotating the line scatterer about the z axis, we record projections $g(p, \varphi, t_1)$ that are modeled by the Radon transform $\mathcal{R}h(x, y, t_1)$. Reconstruction is implemented by the pseudoinverse, $\hat{h}(x, y|t_1) = \mathcal{R}^+ g(p, \varphi|t_1)$, which when computed for all t_1 gives $\hat{h}(x, y, t_1)$. The psf at location x, y, z_0 is $\mathrm{psf}(t_1) = \hat{h}(t_1|x, y)$. The Radon transformation operator $\mathcal{R}$ maps information in object coordinates x, y, z_0 into data coordinates p, φ, t_1, while the inverse operator $\mathcal{R}^+$ maps them back.

at time $t_1 = \ell T$, for integer $1 \le \ell \le L$ and at constant interval T. The t_1 axis is approximately proportional to the image depth axis z via $t_1 = 2z/c$ for sound speed c. Cross-range echo sampling corresponds to the lateral p axis of the array in Fig 1. We have $t_2 = mLT$ for M lines per frame and $-M/2 \le m \le M/2$. The t_2 axis is proportional to the lateral image axis p via $t_2 = pLT/X$, $p = mX$, and array pitch X. For the 1-D arrays in Fig 1, the elevational axis is a point at $q = 0$, and so we set $t_3 = rMLT$ for $1 \le r \le R$ to track the time between frames, MLT, for a total acquisition time $t = RMLT$. However, for echo-volume acquisitions using a 2-D linear array, $t_3 = rMLT/Y$ records acquisitions along the q-axis of the 2-D array, and the volumetric frame rate is $1/RMLT$. Conversion from temporal to spatial coordinates using a 1-D array is summarized by the scan-conversion imaging equation,

$$\mathbf{t} = \mathbf{B}\mathbf{x}\,, \qquad \text{or} \qquad \begin{pmatrix} t_1 \\ t_2 \end{pmatrix} = \begin{pmatrix} 2/c & 0 \\ 0 & LT/X \end{pmatrix} \begin{pmatrix} z \\ p \end{pmatrix}\,. \tag{2}$$

Zemp et al.[8] showed that the system impulse response $h(\mathbf{x}, \mathbf{t})$ reduces to the *point spread function, psf,* when the field position of a point scatterer is fixed and a frame is acquired, i.e., $\mathrm{psf}(\mathbf{t}) = h(\mathbf{t}|\mathbf{x})$. Analogously, the *spatial sensitivity function, ssf,* is obtained when acquisition time is fixed and a point reflector is scanned in space, $\mathrm{ssf}(\mathbf{x}) = h(\mathbf{x}|\mathbf{t})$. Also, for *isoplanatic* regions of the beam, the impulse response is shift invariant and, consequently, a function of a single variable, $h(\mathbf{t} - \mathbf{B}\mathbf{x})$. In isoplanatic regions, Eq (1) becomes a convolution in the spatial domain, $g(\mathbf{t}) = [h * f](\mathbf{t}) + n(\mathbf{t})$.

SPIE USE: ____ DB Check, ____ Prod Check, Notes:

Please verify that (1) all pages are present, (2) all figures are acceptable, (3) all fonts and special characters are correct, and (4) all text and figures fit within the margin lines shown on this review document. Return to your MySPIE ToDo list and approve or disapprove this submission.

3. METHOD

3.1 The forward problem

Projections in pulse-echo ultrasound are echo signals reflected from a line scatterer represented by a product of Dirac deltas

$$f(\mathbf{x}) = \delta(x\cos\varphi + y\sin\varphi)\delta(z - z_0)\ . \tag{3}$$

This object function is a line in the x, y plane at depth z_0 that is scanned by an array along the p axis. The line is then rotated about the z axis to angle φ. Consequently, x, y, z are object coordinates, p, φ, t_1 are echo-data coordinates, and there is a mapping among them.

Applying Eq.(3) to (1), and ignoring the noise term, we express the echo signal as a function of φ,

$$g(\mathbf{t}, \varphi) = \int dy \int dx\, h(x, y, z_0, \mathbf{t})\, \delta(x\cos\varphi + y\sin\varphi)\ , \tag{4}$$

where integration is over the entire xy-plane and the results hold only at $z = z_0$. Since shift invariance can be assumed for these conditions, $h(\mathbf{x}, \mathbf{t}) = h(\mathbf{t} - \mathbf{B}\mathbf{x})$. Combining Eqs (2) and (4) gives (see Fig 2),

$$\begin{aligned} g(t_1, t_2, \varphi) &= \int dy \int dx\, h\left(\frac{Xt_2}{LT} - x, 0 - y, \frac{ct_1}{2} - z_0\right) \delta(x\cos\varphi + y\sin\varphi) \\ g(p, \varphi, t_1) &= \int dy \int dx\, h(x, y, \frac{ct_1}{2} - z_0)\ \delta\left[(p - x)\cos\varphi - y\sin\varphi\right] \\ g(\mathbf{s}) \triangleq g(p, \varphi) &= \int d\mathbf{r}\, h(\mathbf{r})\ \delta(p\cos\varphi - \mathbf{r}\cdot\mathbf{n}(\varphi))\ . \end{aligned} \tag{5}$$

The first form of Eq (5) explicitly recognizes that we acquire data in range, cross range, and at different projection angles. The second form performs the convolutional shifts on the delta function instead of h and substitutes p for t_2. The last form of Eq (5) expresses the echo data as a *modified sinogram* for each range time t_1; henceforth the t_1 and z axes are implied. The modification is that the detector does not rotate with the line scatterer, and therefore the delta function depends on $p\cos\varphi$ instead of p as in photon tomography. We have used $\mathbf{s} = (p, \varphi)$ as a position vector in data space. In object space, we indicate field points using position vector $\mathbf{r} = (x, y)$ and line-scatterer orientation using the unit direction vector $\mathbf{n}(\varphi) = (\cos\varphi, \sin\varphi)$. Now interpretation of the expression in terms of projection geometry becomes clear: each echo signal is made up of impulse response contributions that lie along a line connecting the center of the active array aperture to all points on the line scatterer, viz., $p\cos\varphi = \mathbf{r}\cdot\mathbf{n}(\varphi)$ (see Fig 1). Finally, sinogram generation is written compactly using the Radon operator via $g(\mathbf{s}) = [\mathcal{R}\, h](\mathbf{s})$, where $\mathcal{R} : \mathcal{L}_2(\mathbb{R}^2 \to \mathcal{L}_2([0, \pi] \times \mathbb{R})$.

3.2 Backprojection

Barret and Myers[6] showed g can be backprojected by applying the adjoint of the Radon operator, $\mathcal{R}^\dagger$. Since the kernel of $\mathcal{R}$ is real, we have from (5),

$$\left[\mathcal{R}^\dagger\, g\right](\mathbf{r}) = \int_0^\pi d\varphi \int dp\ g(p, \varphi)\ \delta(p\cos\varphi - \mathbf{r}\cdot\mathbf{n}(\varphi))\ . \tag{6}$$

At each φ, $\mathcal{R}^\dagger$ backprojects the 1D data function $g(p, \varphi)$ back into 2D object space by substituting $p\cos\varphi \to \mathbf{r}\cdot\mathbf{n}(\varphi)$. Combining (5) and (6),

$$\begin{aligned} \left[\mathcal{R}^\dagger\mathcal{R}h\right](\mathbf{r}) &= \int_0^\pi d\varphi \int dp\, \delta(p\cos\varphi - \mathbf{r}\cdot\mathbf{n}(\varphi)) \int d\mathbf{r}'\, h(\mathbf{r}')\, \delta(p\cos\varphi - \mathbf{r}'\cdot\mathbf{n}(\varphi)) \\ &= \int_0^\pi d\varphi \int d\mathbf{r}' \frac{1}{|\cos\varphi|^2}\ \delta\left(\frac{(\mathbf{r} - \mathbf{r}')\cdot\mathbf{n}(\varphi)}{\cos\varphi}\right)\ h(\mathbf{r}') \\ &= \int_0^\pi d\varphi \int d\mathbf{r}' \frac{1}{|\cos\varphi|^2}\ \delta\left(\frac{\mathbf{r}'\cdot\mathbf{n}(\varphi)}{\cos\varphi}\right) h(\mathbf{r} - \mathbf{r}'), \end{aligned} \tag{7}$$

SPIE USE: ____ DB Check, ____ Prod Check, Notes:

Please verify that (1) all pages are present, (2) all figures are acceptable, (3) all fonts and special characters are correct, and (4) all text and figures fit within the margin lines shown on this review document. Return to your MySPIE ToDo list and approve or disapprove this submission.

where the last expression is obtained by changing the integration variable $\mathbf{r}' \to \mathbf{r} - \mathbf{r}'$. We also used the relation[6]

$$\delta(y(x)) = \sum_{n=1}^{N} \frac{\delta(x - x_n)}{|y'(x_n)|} \ , \tag{8}$$

where $y(x)$ is a differentiable function of scalar variable x, x_n are roots of $y(x)$, and the derivative $y'(x_n) \neq 0$ is evaluated at each root. If $\mathbf{r}' = (r' \cos\theta, r' \sin\theta)$, where $-\infty < r' < \infty$ and $0 < \theta < \pi$, then the integrand from Eq (7) can be reduced with the help of (8) for variable φ,

$$\begin{aligned} \frac{1}{\cos^2\varphi}\,\delta\left(\frac{\mathbf{r}' \cdot \mathbf{n}(\varphi)}{\cos\varphi}\right) &= \frac{\delta\left[r'(\cos\theta + \sin\theta\tan\varphi)\right]}{\cos^2\varphi} \\ &= \frac{1}{\cos^2\varphi |r' \sin\theta|}\delta(\tan\varphi + \cot\theta) \ = \ \frac{1}{|r'\sin\theta|}\delta(\varphi) \ , \end{aligned} \tag{9}$$

and Eq (7) becomes

$$\left[\mathcal{R}^\dagger \mathcal{R} h\right](\mathbf{r}) = \int d\mathbf{r}' \frac{1}{|r' \sin\theta|}\, h(\mathbf{r} - \mathbf{r}') \ . \tag{10}$$

Thus the combined operator that both projects and backprojects data, $\mathcal{R}^\dagger\mathcal{R}$, (sometime referred to as the *normal operator*) does not restore the system impulse response. Instead is blurs the function we want with another impulse response $|r' \sin\theta|^{-1}$ impose by the geometry of the measurement. Readers may recognize the blur function from photon CT reconstruction except for the $\sin\theta$ factor that results here from our unique measurement geometry.

3.3 The inverse problem

A method that removes the geometric blur is found by applying the pseudoinverse Radon operator $\mathcal{R}^+$ to projections g,[6]

$$\mathcal{R}^+ = (\mathcal{R}^\dagger\mathcal{R})^{-1}\mathcal{R}^\dagger \ . \tag{11}$$

The logic is that $\mathcal{R}^+ g = (\mathcal{R}^\dagger\mathcal{R})^{-1}\mathcal{R}^\dagger\mathcal{R}h = h$. It can be seen that $(\mathcal{R}^\dagger\mathcal{R})^{-1}$ filters g after backprojection.

The pseudoinverse of the Radon operator may be found from its singular-value decomposition,

$$\left[\mathcal{R}^+\right](\mathbf{r}) = \int d\boldsymbol{\rho} \frac{1}{\sqrt{\mu_{\boldsymbol{\rho}}}} u_{\boldsymbol{\rho}}(\mathbf{r})\, v^\dagger_{\boldsymbol{\rho}}(\mathbf{s}) \ ,$$

where $u_{\boldsymbol{\rho}}$ and $v_{\boldsymbol{\rho}}$ are eigenfunctions corresponding to object and data spaces and $\mu_{\boldsymbol{\rho}}$ are the corresponding eigenvalues. Subscript $\boldsymbol{\rho} = (\rho, \xi)$ is the spatial frequency vector conjugate to polar position $\mathbf{r} = (r, \varphi)$. The first step is to find eigenvalues of the normal operator by applying $\mathcal{R}^\dagger\mathcal{R}$ to an eigenfunction in object space. In our case, the object is the impulse response h and the eigenfunction is the Fourier kernel $u_{\boldsymbol{\rho}}(\mathbf{r}) = \exp(j2\pi\boldsymbol{\rho}\cdot\mathbf{r})$. From (10),

$$\begin{aligned} \left[\mathcal{R}^\dagger\mathcal{R}u_{\boldsymbol{\rho}}\right](\mathbf{r}) &= \int d\mathbf{r}' \frac{1}{|r'\sin\theta|} e^{j2\pi\boldsymbol{\rho}\cdot(\mathbf{r}-\mathbf{r}')} \\ &= u_{\boldsymbol{\rho}}(\mathbf{r}) \int_0^\pi d\theta \int dr' |r'| \frac{1}{|r'\sin\theta|} e^{-j2\pi\rho r'\cos(\xi-\theta)} \\ &= u_{\boldsymbol{\rho}}(\mathbf{r}) \int_0^\pi d\theta \frac{1}{|\sin\theta|} \int dr' \ e^{-j2\pi\rho r'\cos(\xi-\theta)} \\ &= u_{\boldsymbol{\rho}}(\mathbf{r}) \int_0^\pi d\theta \frac{1}{|\sin\theta|}\delta(\rho\cos(\xi-\theta)) \ = \ \frac{u_{\boldsymbol{\rho}}(\mathbf{r})}{|\rho\cos\xi|} \ . \end{aligned} \tag{12}$$

SPIE USE: ____ DB Check, ____ Prod Check, Notes:

Please verify that (1) all pages are present, (2) all figures are acceptable, (3) all fonts and special characters are correct, and (4) all text and figures fit within the margin lines shown on this review document. Return to your MySPIE ToDo list and approve or disapprove this submission.

Thus the eigenvalue for $\mathcal{R}^\dagger\mathcal{R}$ corresponding to $u_{\boldsymbol{\rho}}$ is $\mu_{\boldsymbol{\rho}} = |\rho\cos\xi|^{-1}$. Since $u_{\boldsymbol{\rho}}(\mathbf{r})$ is not a null function, the eigenfunction in image space can be defined as $v_{\boldsymbol{\rho}}(\mathbf{s}) = \mathcal{R}u_{\boldsymbol{\rho}}(\mathbf{r})/\sqrt{\mu_{\boldsymbol{\rho}}}$, which is calculated as follows.

$$\begin{aligned} v_{\boldsymbol{\rho}}(\mathbf{s}) &= \sqrt{|\rho\cos\xi|}\int d\mathbf{r}\; e^{j2\pi\boldsymbol{\rho}\cdot\mathbf{r}}\delta(p\cos\varphi - \mathbf{r}\cdot\mathbf{n}(\varphi)) \\ &= \sqrt{|\rho\cos\xi|}\int d\mathbf{r}\; e^{j2\pi\boldsymbol{\rho}\cdot\mathbf{r}}\int dt\; e^{j2\pi t(p\cos\varphi - \mathbf{r}\cdot\mathbf{n}(\varphi))} \\ &= \sqrt{|\rho\cos\xi|}\int dt\; e^{j2\pi tp\cos\varphi}\delta(\boldsymbol{\rho} - t\mathbf{n}(\varphi)). \end{aligned} \tag{13}$$

The argument $\boldsymbol{\rho} - t\mathbf{n}(\varphi)$ is two dimensional. We project the delta function onto two orthogonal axes $(\mathbf{n}(\varphi), \mathbf{n}^\perp(\varphi))$ as in the expression $\delta(\mathbf{r}) = \delta(x)\,\delta(y)$, and we find the product of two delta functions,

$$\delta(\boldsymbol{\rho} - t\mathbf{n}(\varphi)) = \delta[(\boldsymbol{\rho} - t\mathbf{n}(\varphi))\cdot\mathbf{n}(\varphi)]\delta[(\boldsymbol{\rho} - t\mathbf{n}(\varphi))\cdot\mathbf{n}^\perp(\varphi)] = \delta(\rho\,\cos(\xi-\varphi) - t)\;\delta(\rho\,\sin(\xi-\varphi))\;. \tag{14}$$

Substituting Eq.(14) into (13) and applying (8) to the second delta function, we find

$$v_{\boldsymbol{\rho}}(\mathbf{s}) = v_{\boldsymbol{\rho}}(p,\varphi) = \sqrt{\left|\frac{\cos\xi}{\rho}\right|}e^{j2\pi\rho p\cos\varphi}\;\delta(\xi-\varphi). \tag{15}$$

Consequently, the inverse Radon operator is

$$\left[\mathcal{R}^+\right](\mathbf{r}) = \int d\boldsymbol{\rho}\frac{1}{\sqrt{\mu_{\boldsymbol{\rho}}}}u_{\boldsymbol{\rho}}(\mathbf{r})v^\dagger_{\boldsymbol{\rho}}(\mathbf{s}) = \int d\boldsymbol{\rho}\;|\cos\xi|e^{j2\pi\boldsymbol{\rho}\cdot\mathbf{r}}e^{-j2\pi\rho p\cos\varphi}\delta(\xi-\varphi), \tag{16}$$

and therefore

$$\begin{aligned} \hat{h}(\mathbf{r}) &= \left[\mathcal{R}^+ g\right](\mathbf{r}) \\ &= \int_0^\pi d\varphi\int dp\int d\boldsymbol{\rho}\;|\cos\xi|\;e^{j2\pi\boldsymbol{\rho}\cdot\mathbf{r}}e^{-j2\pi\rho p\cos\theta}\delta(\xi-\varphi)g(p,\varphi) \\ &= \int_0^\pi d\varphi\int d\rho\,|\rho|\;e^{j2\pi\rho\mathbf{r}\cdot\mathbf{n}(\varphi)}|\cos\varphi|\int dp\;e^{-j2\pi\rho p\cos\varphi}g(p,\varphi)\;, \end{aligned} \tag{17}$$

where $\boldsymbol{\rho} = \rho\,\mathbf{n}(\xi)$ and $d\boldsymbol{\rho} = |\rho|\,d\rho\,d\xi$ for $-\infty < \rho < \infty$ and $0 < \xi \le \pi$.

Eq (17) is similar to the expression for conventional filtered backprojection methods.[7] The difference is the factor $\cos\varphi$ in the expression $|\cos\varphi|\int dp\,\exp(-j2\pi\rho p\cos\varphi)\,g(p,\varphi)$ that doesn't appear in CT reconstructions. This expression is the 1-D spatial Fourier transform of g, to which the ramp filter

$$w(\mathbf{r},\varphi) \triangleq w(\mathbf{r}\cdot\mathbf{n}(\varphi)) = \int d\rho\,|\rho|\;e^{j2\pi\rho\mathbf{r}\cdot\mathbf{n}(\varphi)} \tag{18}$$

is applied and the results for each projection angle are summed to reconstruct the impulse response $\hat{h}$. The main limitation in our experiment is that the integration variable p is scaled depending on the rotation angle of the line scatterer. As φ increases from 0 to $\pi/2$, the length of the $p\cos\varphi$ axis decreases from typically 40 mm to 0 mm. One solution is to project $g(p,\varphi)$ onto the $\mathbf{n}(\varphi)$ axis so that the p axes at each angle are the same, and then to apply a standard inverse Radon transform. If the p axis was continuously sampled, all information would be recovered with this approach. However p is sampled on an interval equal to the array pitch, $X = 0.2$ mm, i.e., $p = mX$, where typically $M = 192$, and therefore information is lost increasingly as $\varphi \to \pi/2$. In the next section, we frame another approach that preserves more of the information.

SPIE USE: ____ DB Check, ____ Prod Check, Notes:

Please verify that (1) all pages are present, (2) all figures are acceptable, (3) all fonts and special characters are correct, and (4) all text and figures fit within the margin lines shown on this review document. Return to your MySPIE ToDo list and approve or disapprove this submission.

3.4 Numerical implementation

We replace $\mathbf{r} \to (x, y)$ and $\mathbf{n}(\varphi) \to (\cos\varphi, \sin\varphi)$, and acknowledge that the line-scatterer angle is discrete $\varphi_n = \pi(2n-1)/180$ for $1 \le n \le 90$. For the moment, also set $|\rho| = 1$. Then we can combine Eqs (18) and (17) to find the unfiltered backprojection estimate h_u,

$$\begin{aligned} \hat{h}_u(x,y) &= \sum_n \int d\rho \; e^{j2\pi\rho(x\cos\varphi_n + y\sin\varphi_n)} |\cos\varphi_n| \; G(\rho\cos\varphi_n, \varphi_n) \\ &= \sum_n \hat{h}_u(x,y,\varphi_n) \; . \end{aligned} \tag{19}$$

We define

$$G(\rho\cos\varphi_n, \varphi_n) = \int dp \; e^{-j2\pi\rho p\cos\varphi_n} \; g(p, \varphi_n) \tag{20}$$

as the 1D spatial Fourier transform, and $\hat{h}_u(x, y, \varphi_n)$ as the unfiltered backprojection result for angle φ_n, which can be written as

$$\begin{aligned} \hat{h}_u(x,y,\varphi_n) &= \int d(\rho\cos\varphi_n) \; e^{j2\pi\rho(x\cos\varphi_n + y\sin\varphi_n)} \; G(\rho\cos\varphi_n, \varphi_n) \\ &= \int d\rho' \; e^{j2\pi\rho'(x + y\tan\varphi_n)} \; G(\rho', \varphi_n) \\ &= g(x + y\tan\varphi_n, \varphi_n) \; , \qquad \text{where } \; \rho' = \rho\cos\varphi_n \; . \end{aligned} \tag{21}$$

Eq (21) describes how to take 1-D projection data and create one unfiltered backprojection line. If we have a 2-D array, then we can obtain projections along the p and q data axes (Fig 1) that correspond to the x and y object axes. The relation between $g(x + y\tan\varphi_\mathrm{n}, \varphi_\mathrm{n})$ and 2-D array scanning is described as follows,

$$\begin{aligned} g(x + y\tan\varphi_\mathrm{n}, \varphi_\mathrm{n}) &= \int\int dx'dy'h(x',y')\delta((x + y\tan\varphi_\mathrm{n})\cos\varphi_\mathrm{n} - x'\cos\varphi_\mathrm{n} - y'\sin\varphi_\mathrm{n}) \\ &= \int\int dx'dy'h(x',y')\delta((x - x')\cos\varphi_\mathrm{n} + (y - y')\sin\varphi_\mathrm{n}) \\ &= g(x, y, \varphi_n) \; , \end{aligned} \tag{22}$$

and the reconstruction is straightforward. However, the limitation for our experiment is that a 1-D array does not naturally sample the object along the q axis (in elevation). Without y-axis information, the best we can do is interpolate.

Recall that the p axis is sampled, $p = mX$ for $-M/2 \le m \le M/2$, where the pitch of the array is $X = 0.2$ mm and there are $M = 192$ total array elements and 192 projections. We will adopt the same sampling interval for the y axes, such that $x = mX$ and $y = m'X$, and, as described above, φ_n is from 1° to 179° in steps of 2°. So as we step along m and m' in $\hat{h}_u(m, m', \varphi_n)$, we go to $g(m + m'\tan\varphi_n, \varphi_n)$ for values using interpolation. However, values of $m'\tan\varphi_n$ that extend outside the range $-M/2 \le m' \le M/2$ must be set to zero because we have no values to interpolate, and information is lost.

The last two steps of the process are to apply a 1-D ramp filter $w(\mathbf{r}, \varphi_n)$ from Eq (18) to each $\hat{h}_u(\mathbf{r}, \varphi_n)$ line, i.e., remove the earlier assumption that $|\rho| = 1$, and then sum the results over all angles:

$$\hat{h}(\mathbf{r}) = \sum_{\varphi_n} [w * \hat{h}_u](\mathbf{r}) = \left[w_{2D} * \sum_{\varphi_n} \hat{h}_u \right](\mathbf{r}) \; . \tag{23}$$

The second form is preferred because it is computationally faster and mathematically equivalent to apply a 2-D ramp filter to the summation once, rather than applying a 1-D filter to each line. The process is repeated for each range time t_1 to build up a 3-D reconstruction of the impulse response $\hat{h}(x, y, t_1)$, as we show in Fig 2, but keep in mind that the results are for a single depth, $z = z_0$. If we repeat the experiment for different depths, we can find $\hat{h}(x, y, z, t_1) \simeq h(\mathbf{x}, \mathbf{t})$, which approximates the full spatiotemporal pulse-echo impulse response for the ultrasonic imaging system.

SPIE USE: ____ DB Check, ____ Prod Check, Notes:

Please verify that (1) all pages are present, (2) all figures are acceptable, (3) all fonts and special characters are correct, and (4) all text and figures fit within the margin lines shown on this review document. Return to your MySPIE ToDo list and approve or disapprove this submission.

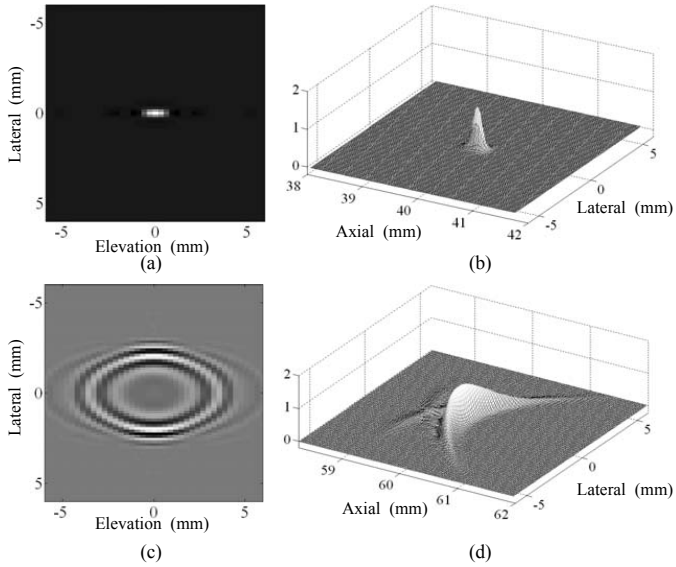

Figure 3. 3-D pulse-echo impulse responses are simulated in Field II at the focal length (a,b) positioned at (0, 0, 40 mm) and in the far field (c,d) positioned at (0, 0, 60 mm). (a) and (c) display responses in the x (lateral), y (elevational) plane; the pressure amplitude is indicated by gray-scale values. (b) and (d) display the responses in the x (lateral) and $ct_1/2$ (axial) plane; the magnitude of the demodulated pulse is indicated by height in the 3-D plot. These modeled pulses are input to a program simulating $g(p, t_1, \varphi)$ projection, and therefore serve as the ground truth for comparing pulse reconstructions.

4. RESULTS AND DISCUSSIONS

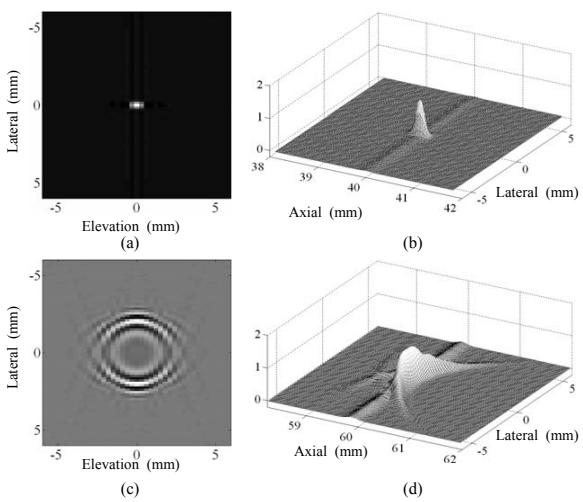

Figure 4. Reconstructed impulse responses where the models of Fig 3 were applied to simulate echo projections acquired along the p axis only (data from a 1-D array).

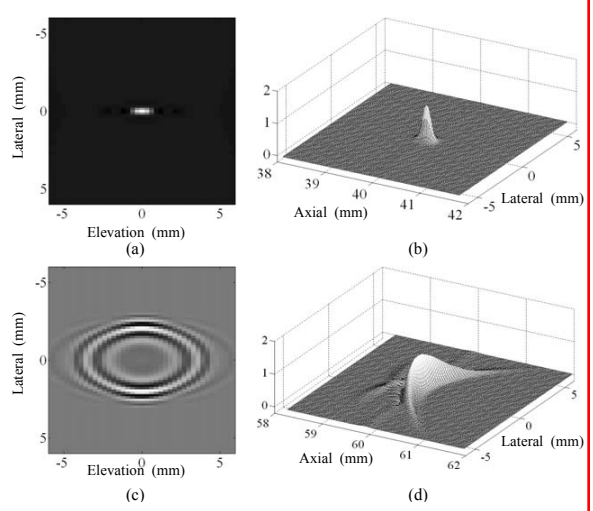

Figure 5. Reconstructed impulse responses where the models of Fig 3 were applied to simulate echo projections acquired along the p and q axes (data from a 2-D array).

4.1 Simulation

We applied the Field II Ultrasound Simulation Program[9,10] to model 3-D impulse responses with typical system parameters of a Siemens Sonoline Antares system (Mountain View, CA). The VF10-5 1-D linear array transducer was modeled. We simulated echo projections $g(p, t_1, \varphi)$ or $g(p, q, t_1, \varphi)$ from the modeled impulse responses $h(\mathbf{x}, t_1)$ and verified the reconstructions by comparisons to the original Field II models. The same system parameters were applied to obtain the experimental results shown below.

The system parameters used to model the impulse response are as follows. Range time $t_1 = \ell T$ is sampled at 40 Msample/s ($T = 25$ ns and therefore the spatial range sampling is $cT/2 = 0.019$ mm for $c = 1487$ m/s). The lateral sampling interval, $X = 0.2$ mm, equals the element pitch. We set a 40-mm transmit/receive

7629 - 14 V. 2 (p.8 of 11) / Color: No / Format: A4 / Date: 2010-02-16 12:42:59 PM

SPIE USE: ____ DB Check, ____ Prod Check, Notes:

Please verify that (1) all pages are present, (2) all figures are acceptable, (3) all fonts and special characters are correct, and (4) all text and figures fit within the margin lines shown on this review document. Return to your MySPIE ToDo list and approve or disapprove this submission.

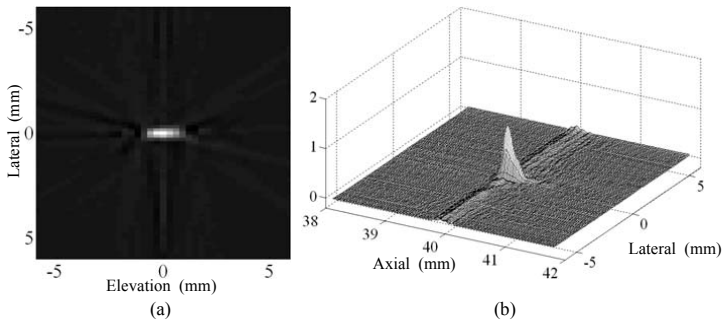

Figure 6. A 3-D impulse response as reconstructed from experimental data at 7 MHz. (a) and (b) are experimental analogs of the simulation results in Fig 3 (a) and (b).

focal length and a 96-element (∼20 mm) active aperture. The array has 192 total elements separated by a 0.02 mm kerf. The elevational element length is $Y = 25$ mm. We applied a two-cycle excitation voltage to the transducer and found a nearly Gaussian-shaped pulse-echo amplitude spectrum with a 53% bandwidth that is centered at ∼7 MHz. With these parameters, we generated impulse responses at spatial positions $\mathbf{x} = (0,\ 0,\ 40\ \text{mm})$ and $(0,\ 0,\ 60\ \text{mm})$ corresponding, respectively, to the focal length and far field of an f/2 in-plane aperture, Fig 3. Since the responses are three dimensional, we display the pressure amplitudes separately in the axial-lateral $(ct_1/2, x)$-plane and the lateral-elevational (x, y)-plane.

To approximate "continuous" impulse responses while generating projections, we sampled functions in Field II at 15 times the rates indicated above. Projection data for a 1-D array, as shown in Fig 1, and a symmetric 2-D array, where projections are recorded along both the p and q axes, were simulated separately. In each case, projections were acquired at 90 angular locations, $1^{\circ} \leq \varphi \leq 179^{\circ}$ and no measurement noise was added.

The 2-D array recordings, Fig 5, provide excellent reconstructions of model pulses, Fig 3, with only minor errors. However, reconstructions using projections from the 1-D array, Fig 4, show significant distortions. Clearly the missing data from the elevational axis for 1-D arrays limits reconstruction accuracy. Although the overall mean square errors with respect to Fig 3 are small (0.12% for the pulse at the focal length and 0.32% for the pulse in the far field), the missing data from the elevational axis generates artifacts along the axial and elevational axes that are more significant in the far field than at the focal length.

4.2 Experiment results

We recorded measured RF echo signals $g(p, t_1, \varphi)$ by fixing a line scatterer and rotating a linear array transducer that was mounted in a fixture that provide positioning accuracy. The line scatterer was a 0.12-mm-dia metal wire placed in degassed water at room temperature. All of the system parameters and geometric details described above for simulations were applied experimentally. Dynamic focusing and aperture growth were disabled on the system. The echo SNR of the system relative to the wire echo was approximately 32 dB for each recorded frame. However, at each angle, we acquired 100 RF frames that were averaged to reduce the effects of electronic noise. The echo SNR for the averaged projections increased to 52 dB, and thus we considered the RF data to be noiseless.

The reconstructed impulse response for the measurement at the 40-mm focal length is shown in Fig 6 (a) and (b). Compared with the corresponding simulation results of Fig 4 (a) and (b), the experimental results are similar. Differences are likely due to small discrepancies in the assumed array properties or misalignment between the beam axis and line scatterer. Such variations increase the error in the elevational response shown in Fig 6 (b). Some ringing of the pulse interacting with the wire scatterer is evident.

We do not know the true impulse response for the experimentally recorded data, so we must verify the reconstruction another way. Our $\hat{h}$ estimate is evaluated by studying its ability to decorrelate the system

7629 - 14 V. 2 (p.9 of 11) / Color: No / Format: A4 / Date: 2010-02-16 12:42:59 PM

SPIE USE: ____ DB Check, ____ Prod Check, Notes:

Please verify that (1) all pages are present, (2) all figures are acceptable, (3) all fonts and special characters are correct, and (4) all text and figures fit within the margin lines shown on this review document. Return to your MySPIE ToDo list and approve or disapprove this submission.

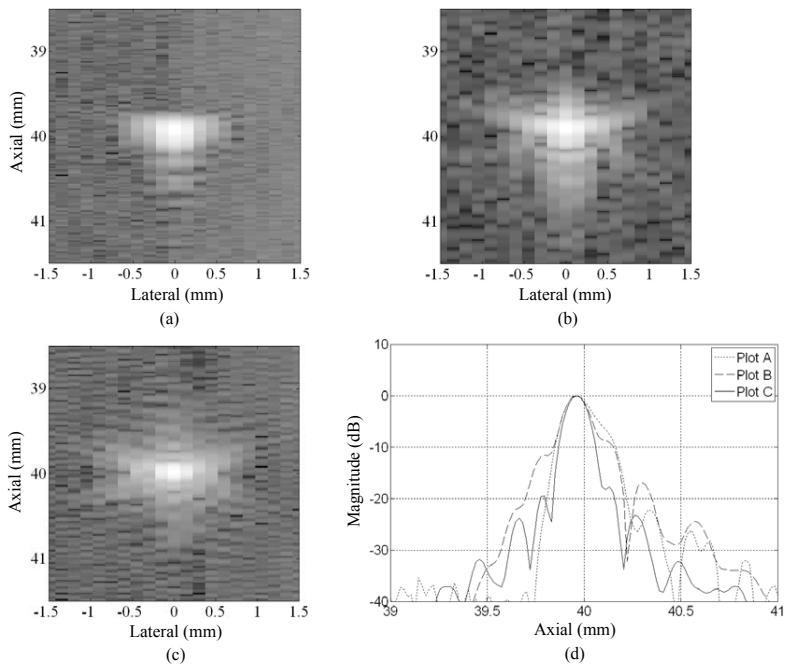

Figure 7. (a) B-mode image (log compressed) of a wire target, $\varphi = 0^o$. (b) B-mode image (log compressed) of the same wire target but where the RF signals were Wiener filtered assuming the system impulse response simulated by the Field II program in Fig 3. (c) Same as (b) but applying the system impulse response reconstructed from experimental data. (d) Three center columns (normalized) of the B-mode images: Plot A (the dot line) is the center column of the standard B-mode image (a), Plot B (the dash line) is the center column of the Wiener filtered B-mode image with the field II impulse response, and Plot C (the solid line) is the center column of the Wiener filtered B-mode image with our reconstructed impulse response.

response from the RF echo signals of a wire target aligned along the y axis. The B-mode image obtained from the system is displayed in Fig 7 (a). Decorrelation was implemented by constructing a Wiener filter, as described previously,[4] that is based on the impulse response of the system and SNR estimates. Successful decorrelation results in a B-mode image of the wire target where the reflected sound energy is concentrated as much as possible in a small region. Applying the modeled impulse response from Fig 3 to the Wiener filter to the RF frame and then computing the envelope and scan converting the data gives the image of Fig 7 (b). Following the same process but now applying the reconstructed impulse response from measured data gives the image of Fig 7 (c). Center columns of the three B-mode images are plotted in Fig 7 (d). The plot shows the width of main lobe in Fig 7 (c) has a substantial reduction in comparison with that of the standard B-mode image in Fig 7 (a). Besides, Wiener filtering with our reconstructed impulse response can remove some ringing effects from the standard B-mode images, that we could not do with the Field II impulse response. It is shown that the experimental reconstruction results in the most concentrated main-lobe signal energy and the most symmetric response.

5. SUMMARY AND CONCLUSIONS

We have reported on an analytical method to reconstruct the pulse-echo impulse response of an ultrasound imaging system from the RF echo data of a rotating line scatterer. Applying a linear-systems approach to modeling the formation of echo-signal projections from a line source, we developed an inverse operator that results in a modified filtered backprojection algorithm. The modification accounts for specific properties of the measurement and detector geometries. If we are able to record projection data in a plane, as occurs with a 2-D linear array transducer, we find that the impulse responses can be accurately reconstructed. However,

7629 - 14 V. 2 (p.10 of 11) / Color: No / Format: A4 / Date: 2010-02-16 12:42:59 PM

SPIE USE: ____ DB Check, ____ Prod Check, Notes:

Please verify that (1) all pages are present, (2) all figures are acceptable, (3) all fonts and special characters are correct, and (4) all text and figures fit within the margin lines shown on this review document. Return to your MySPIE ToDo list and approve or disapprove this submission.

projections recorded along a line, as occurs naturally with 1-D arrays, fail to capture essential information, which results in reconstruction artifacts. Artifacts increase for impulse responses measured far from the focal length of the aperture. Scanning a 1-D array mechanically along the elevational direction (y axis) recovers much of the information.

This technique can be used to estimate the pulse-echo impulse response throughout the imaging field. It may also be useful for measuring pulse distortions in aberrating media. We intend to explore its use in beamforming methods involving spatial filtering techniques.[4]

ACKNOWLEDGMENTS

The authors are grateful to P. Scott Carney from Electrical and Computer Engineering Department, University of Illinois at Urbana-Champaign for several helpful discussions. This work is supported by NIH under award No. CA118294.

REFERENCES

[1] R.S.C. Cobbold, *Foundations of Biomedical Ultrasound*. New York, NY: Oxford Univ Press, 2006.

[2] T. Taxt, "Restoration of medical ultrasound images using two-dimensional homomorphic deconvolution," *IEEE Trans Ultrason Ferro Freq Control*, 42:543-554, 1995.

[3] O.V. Michailovich and D. Adam, "A novel approach to the 2D blind deconvolution problem in medical ultrasound," *IEEE Trans Med Imag*, vol. 24, no. 1, pp. 86-104, 2005.

[4] C.K. Abbey, R.J. Zemp, J. Liu, K.K Lindfors, and M.F. Insana, "Observer efficiency in discrimination tasks simulating malignant and benign breast lesions with ultrasound," *IEEE Trans Med Imag*, vol. 25, no. 2, pp. 198-209, 2006.

[5] R.F. Wagner, S.W. Smith, J.M. Sandrik, and H. Lopez, "Statistics of speckle in ultrasound B-scans," *IEEE Trans Sonics Ultrason*, vol. 30, no. 3, pp. 156-163, 1983.

[6] H.H. Barrett, K.J. Myers, *Foundations of Image Science*, John Wiley & Sons, Hoboken, NJ, 2004.

[7] A.C. Kak, M. Slaney, *Principles of Computerized Tomographic Imaging*, Society of Industrial and Applied Mathematics, Philadelphia, PA, 1999.

[8] R.J. Zemp, C.K. Abbey, M.F. Insana, "Linear system model for ultrasonic imaging: application to signal statistics," *IEEE Trans Ultrason Ferro Freq Control*, 50:642-54, 2003.

[9] J.A. Jensen and N. B. Svendsen, "Calculation of pressure fields from arbitrarily shaped, apodized, and excited ultrasound transducers," *IEEE Trans Ultrason Ferro Freq Control*, 39:262-267, 1992.

[10] J.A. Jensen, "Field: A program for simulating ultrasound systems," *Med Biol Eng Computing*, 34:351-353, 1996.

7629 - 14 V. 2 (p.11 of 11) / Color: No / Format: A4 / Date: 2010-02-16 12:42:59 PM

SPIE USE: ____ DB Check, ____ Prod Check, Notes: